LETTER

Corrected: Author Correction

https://doi.org/10.1038/s41586-018-0855-y

Spatially resolved steady-state negative capacitance

Ajay K. Yadav[1,12], Kayla X. Nguyen[2,12], Zijian Hong[3,12], Pablo García-Fernández[4,12], Pablo Aguado-Puente[5], Christopher T. Nelson[6,7], Sujit Das[7], Bhagwati Prasad[7], Daewoong Kwon[1], Suraj Cheema[7], Asif I. Khan[1,11], Chenming Hu[1], Jorge Íñiguez[8], Javier Junquera[4], Long-Qing Chen[3], David A. Muller[9,10], Ramamoorthy Ramesh[7] & Sayeef Salahuddin[1]*

Negative capacitance is a newly discovered state of ferroelectric materials that holds promise for electronics applications by exploiting a region of thermodynamic space that is normally not accessible[1–14]. Although existing reports of negative capacitance substantiate the importance of this phenomenon, they have focused on its macroscale manifestation. These manifestations demonstrate possible uses of steady-state negative capacitance—for example, enhancing the capacitance of a ferroelectric–dielectric heterostructure[4,7,14] or improving the subthreshold swing of a transistor[8–12]. Yet they constitute only indirect measurements of the local state of negative capacitance in which the ferroelectric resides. Spatial mapping of this phenomenon would help its understanding at a microscopic scale and also help to achieve optimal design of devices with potential technological applications. Here we demonstrate a direct measurement of steady-state negative capacitance in a ferroelectric–dielectric heterostructure. We use electron microscopy complemented by phase-field and first-principles-based (second-principles) simulations in $SrTiO_3/PbTiO_3$ superlattices to directly determine, with atomic resolution, the local regions in the ferroelectric material where a state of negative capacitance is stabilized. Simultaneous vector mapping of atomic displacements (related to a complex pattern in the polarization field), in conjunction with reconstruction of the local electric field, identify the negative capacitance regions as those with higher energy density and larger polarizability: the domain walls where the polarization is suppressed.

When a material transitions to a ferroelectric phase, it develops a stable polarization state that is doubly degenerate[1] (Fig. 1a), corresponding to positions of minima (A and B in Fig. 1a) in its free-energy (G) landscape[1]. At these stable states, the curvature of the free energy is positive, that is, $\partial^2G/\partial D^2 > 0$, indicating positive permittivity ($\epsilon \propto (\partial^2G/\partial D^2)^{-1}$), where D is the electric displacement field. These equilibrium states are separated by a region where the curvature is negative ($\partial^2G/\partial D^2 < 0$), defining a region of negative permittivity (highlighted as the region between H and K in[2] Fig. 1a, b). It is possible to stabilize the ferroelectric in this negative permittivity region by adding, to its double-well structure, the parabolic energy landscape of a normal dielectric (Fig. 1b). Accessing such 'forbidden' regions of the thermodynamic landscape of ferroic materials at equilibrium remains a challenge in condensed matter physics. In addition to providing key insights into fundamental physics, such a steady-state negative capacitance has implications for lowering the energy consumption in conventional electronics (the 'Boltzmann tyranny'[2,5]). However, the exploration of negative capacitance has been constrained by the thermodynamic requirement that, in a physical system, the capacitance is always positive—which has meant that the emergence of negative capacitance could be probed only indirectly, through an observation of capacitance enhancement[4,7,14]. To probe the state of negative capacitance directly, the polarization and electric fields internal to the material need to be measured locally. In addition, the 'double-well' concept described above is only representative of a single-domain scenario. So it is important to examine how this will change in presence of more than one domain[14,15]. Here we use $SrTiO_3/PbTiO_3$ superlattices as a model system that breaks into vortex-like domains[16–18], as discussed in detail below. We find that local regions of negative capacitance emerge at the domain walls, where the polarization is suppressed. In addition, we find that these walls are also the regions where the energy density is larger than that in the bulk of the domains where the polarization is not suppressed. From this variation of the energy densities, we infer negative curvature ($\partial^2G/\partial D^2 < 0$) within the domain walls, in close resemblance to the 'double well' model. This is shown schematically in Fig. 1c.

We use superlattices of $SrTiO_3/PbTiO_3$ as our model ferroelectric–dielectric heterostructure system in which a state of negative capacitance is expected to be stabilized at equilibrium. In such superlattices, vortex-like topologies[16,17] are observed as the dominant polarization pattern when the periodicity is optimal[18,19] (see also supplementary information of ref. [20]). The defining characteristic of these topologies is the gradual suppression of polarization near the centre of the vortex. Occurrence of such vortex structures in a displacive ferroelectric such as $PbTiO_3$ enables us to perform detailed measurements of the local

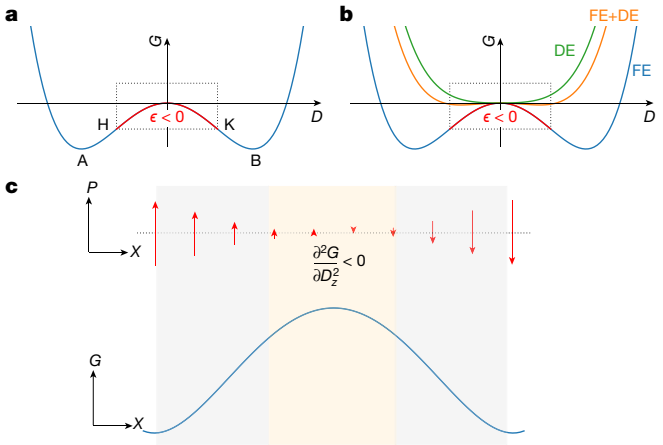

Fig. 1 | Steady-state negative capacitance. a, Free energy landscape for a ferroelectric (FE) material. G, free energy; D, displacement. **b**, Free energy landscape for a ferroelectric–dielectric (FE–DE) heterostructure. A and B are the minimum energy points in a single ferroelectric. H and K define the boundary of the region where the permittivity ϵ is negative. **c**, Spatially resolved energy density in a multi-domain system (bottom) juxtaposed with the variation in polarization P (top). The domain walls where the polarization is suppressed have greater energy density than the bulk domain.

[1]Department of Electrical Engineering and Computer Sciences, University of California, Berkeley, CA, USA. [2]Department of Chemistry and Chemical Biology, Cornell University, Ithaca, NY, USA. [3]Department of Materials Science and Engineering, Pennsylvania State University, State College, PA, USA. [4]Departamento de Ciencias de la Tierra y Física de la Materia Condensada, Universidad de Cantabria, Cantabria Campus Internacional, Santander, Spain. [5]Atomistic Simulation Centre, Queen's University Belfast, Belfast, UK. [6]National Center for Electron Microscopy, Lawrence Berkeley Laboratory, Berkeley, CA, USA. [7]Department of Materials Science and Engineering, University of California, Berkeley, CA, USA. [8]Materials Research and Technology Department, Luxembourg Institute of Science and Technology, Esch/Alzette, Luxembourg. [9]School of Applied and Engineering Physics, Cornell University, Ithaca, NY, USA. [10]Kavli Institute at Cornell for Nanoscale Science, Cornell University, Ithaca, NY, USA. [11]Present address: School of Electrical and Computer Engineering, Georgia Institute of Technology, Atlanta, GA, USA. [12]These authors contributed equally: Ajay K. Yadav, Kayla X. Nguyen, Zijian Hong, Pablo García-Fernández. *e-mail: sayeef@berkeley.edu

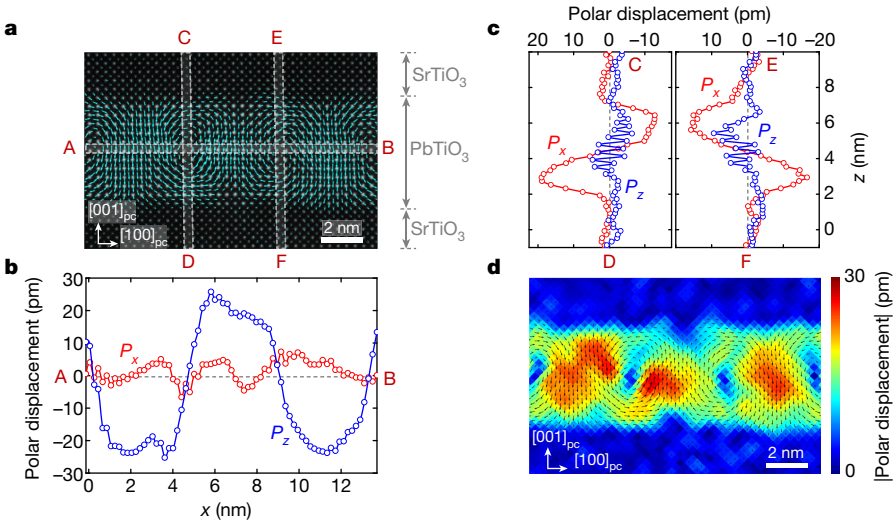

Fig. 2 | Identifying the regions of negative permittivity. a, Overlay of the polarization vector map (indicated by the cyan vectors) on a cross-sectional HAADF-STEM image of a $PbTiO_3$ layer embedded within a $(SrTiO_3)_{12}/(PbTiO_3)_{12}$ superlattice. **b**, Variation in the x and z components of polarization (P_x and P_z, respectively) along a horizontal line (A–B, see **a**) passing through the cores of the vortices. **c**, Line profiles showing the variation in P_x and P_z along two vertical lines (C–D and E–F; see **a**) passing through the cores of the vortices. **d**, A 2D colour map showing the variation in the magnitude of polar displacements (for the same sub-region shown in **a**) with an overlay of the polarization vector map (indicated by black vectors).

configuration of the polarization using scanning transmission electron microscopy (STEM) techniques[21–23] (see also supplementary information of ref. [22]). For a $(SrTiO_3)_{12}/(PbTiO_3)_{12}$ superlattice, polar atomic displacement vectors ($\boldsymbol{P}_{PD}$), when extracted from atomic-resolution STEM images[18,23,24], reveal stabilization of a well-defined array of clockwise and anticlockwise rotating polarization patterns (Fig. 2a). The spatial variation of the polarization along the horizontal and vertical axes are shown in Fig. 2b, c. The suppression of polarization near the vortex core becomes more apparent when a two-dimensional (2D) map of the magnitude ($|\boldsymbol{P}_{PD}|$) is plotted (Fig. 2d), corresponding to the polarization region detailed in Fig. 2a. In these regions of suppressed polarization, we expect the material to be in a relatively high energy state, which suggests that these vortex cores should exhibit negative permittivity.

To test this hypothesis, we used STEM in conjunction with the newly developed electron microscopy pixel array detector (EMPAD)[23], which records the full momentum distribution at every scan position, providing sufficient information to simultaneously measure the polar order and electric field. Here, convergent beam electron diffraction (CBED) mapping of the probability current flow ($\langle \boldsymbol{p} \rangle$) of conjugate disks of superlattice material, oriented (200)/($\bar{2}$00) and (020)/(0$\bar{2}$0), quantitatively measures the polarization field (Fig. 3a) in a $(SrTiO_3)_{12}/(PbTiO_3)_{12}$ superlattice (described in detail in Methods section 'EMPAD'). The polarization field reproduces the same vortex structures (Fig. 3a) as those obtained by an independent, Z-contrast, high-resolution STEM (HRSTEM) technique (Fig. 2a). To reconstruct the macroscale electric field (Fig. 3b), we note that the average electric field $E(r_0)$ is equal to the average field over the volume of the crystal cell V_c that contains the lattice point r_0:

$$E(r_0) = \frac{1}{V_c}\int e(r)\mathrm{d}V \quad (1)$$

where $e(r)$ is a microscale field defined to be the nuclear field of the atom and dV is the volume over which the polarity is measured (see Methods section 'EMPAD' for details).

Our technique is most robust away from the interfaces, because it is least affected by offsets there. Therefore, we focus on the line A–B in Fig. 2a, which goes roughly through the middle of the ferroelectric layer. Also, along this line the x components of the polarization and electric field are negligible and so we can simply look at the z components. Figure 3c shows the experimentally measured z component of the polarization (P_z) and electric field (E_z) along this line. The magnitude of the measured polarization was calibrated using the spontaneous polarization of $PbTiO_3$[25]. The polarization changes from full-length-up to full-length-down through regions of suppressed polarization including zero. This allows us to extract E_z, which in this case is the internal field (E_{int}) because there is no externally applied bias, as a function of P_z. We note that the extraction of this functional dependence is an approximation (a local relation is assumed). However, this

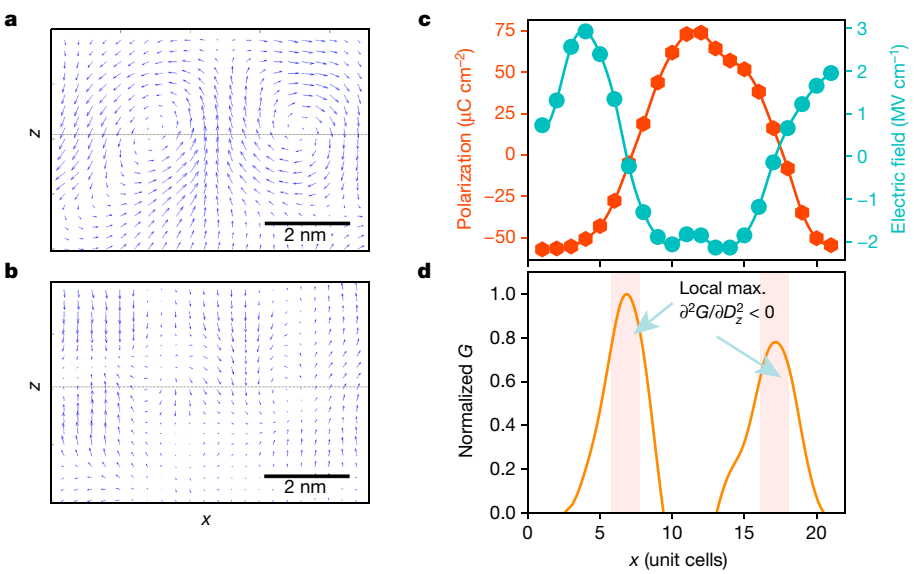

Fig. 3 | Measurement of local electric field and polarization field using EMPAD-STEM. a, Polarization vector map from a sub-region of a $PbTiO_3$ layer embedded within a $(SrTiO_3)_{12}/(PbTiO_3)_{12}$ superlattice as measured using STEM (details in Methods, Extended Data Figs. 1 and 2). **b**, Local electric field in a $PbTiO_3$ layer (corresponding to the same region shown in **a**) as measured using TEM. **c**, Variation in the z components of local polarization (P_z; red hexagons) and electric field (E_z; blue circles) along a horizontal line (indicated by the horizontal lines in **a** and **b**) that passes through the core of the vortices. **d**, Local energy density estimated from the variation in P_z and E_z along the same line. Regions around the core (arrowed) have negative curvature ($\partial^2 G/\partial D^2 < 0$). See details in Methods sections 'Estimation of the free energy (G)' and 'Estimation of the permittivity'.

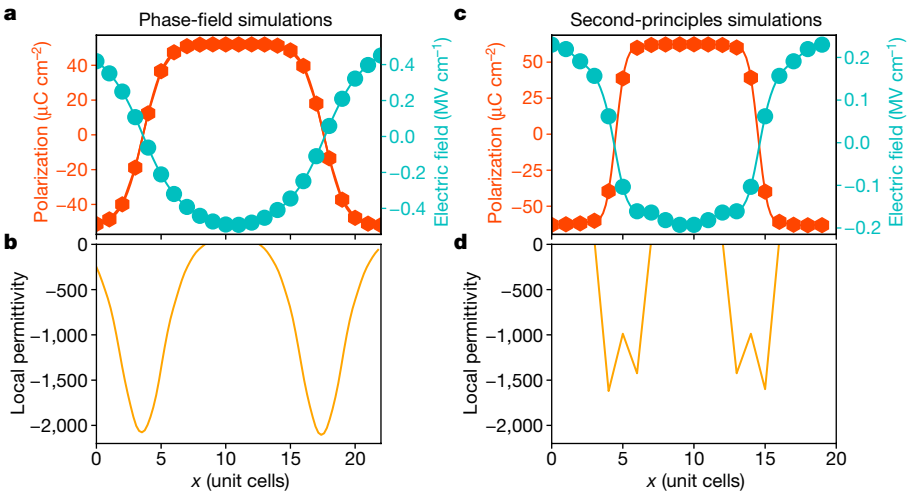

Fig. 4 | Local permittivity calculated using second-principles and phase-field simulations. Phase-field simulations and second-principles simulations were performed for a $(SrTiO_3)_n/(PbTiO_3)_n$ superlattice to obtain local polarization and electric field distributions within ferroelectric and dielectric layers of the superlattice structure. Polarization patterns from both second-principles ($n = 10$) and phase-field simulations ($n = 12$) show the presence of vortex topologies. **a**, The variation in P_z (red hexagons) and E_z (blue circles) predicted from phase-field simulations (along a horizontal line that passes through the core of the vortices). For details, see Methods and Extended Data Fig. 3. **b**, Corresponding variation in the z component of local permittivity extracted from local P_z and E_z predicted from phase-field simulations (see Methods). **d**, **e**, As **a**, **b**, but using second-principles calculations.

approximation is well justified by the fact that if we look into individual vortices, the E_z versus P_z dependence remains similar within the experimental resolution. We next find the displacement from $D_z = \epsilon_0 E_z + P_z$ and the free energy from $G \approx \int E_z \mathrm{d}D_z$ (see Methods section 'Estimation of the free energy (G)' and Extended Data Fig. 7a, b for details). This estimated G as a function of D_z shows a clear negative curvature $\partial^2 G/\partial D^2 < 0$ near the regions where D_z is small. Therefore, the spatial mapping of the polarization and the electric field shows local regions of the ferroelectric stabilized in a state where $\partial^2 G/\partial D^2$ is estimated to be negative. We can further correlate the values of D_z according to its occurrence along the x direction. This gives a mapping of the local energy densities along the x direction, as shown in Fig. 3d. The shape and amplitude of the energy density function look very similar from core to core. On the basis of this analysis, we expect that local regions of negative permittivity will appear in the regions at and near the core. Currently EMPAD measurements cannot be done in the presence of an externally applied field. Nonetheless, considering the fact that, in a capacitor measurement, the externally applied bias would be very small, it is possible to estimate permittivity near the core, assuming this external bias to be a small perturbation. Extended Data Fig. 8 shows permittivity estimated in this manner, and we indeed find negative permittivity around the core (see Methods section 'Estimation of the permittivity' for details). These estimations from the experimental measurement are validated by both phase-field and first-principles-based (which we term 'second-principles') calculations where it is possible to apply a field and directly calculate the response function. As shown in Fig. 4b, d, the permittivity is found to be negative in the regions near the core. Furthermore, a full 2D mapping of the local energy densities from second-principles calculations, shown in Extended Data Fig. 6, demonstrates that this negative permittivity appears at the regions of higher energy density, exactly as it is estimated from the experiment in Fig. 3d. Finally, for a self-consistent check, we measured the macroscale capacitance of these superlattices. Compared to the capacitance of the constituent $SrTiO_3$, the superlattice shows an enhancement of 3.7 times in capacitance, a hallmark of stabilization of the ferroelectric layer at a state of negative capacitance (see Methods section 'Macroscale capacitance measurement' and Extended Data Fig. 9). Within this voltage range (-1 V to $+1$ V), we did not see any hysteresis.

The details of the calculations performed using phase-field and second-principles methods are provided in Methods sections 'Phase-field simulations', 'Second-principles calculations' and 'Estimation of the free energy (G)'. Extended Data Fig. 3 shows detailed polarization and electric field vector-maps from the phase-field calculations. In accordance with Fig. 3, in Fig. 4a we plot P_z and E_z along a line that goes through the cores of the vortices. The behaviour of both P_z and E_z strongly resembles the experimental data in Fig. 3c. A similar conclusion is arrived at from the second-principles ab initio calculations in Fig. 4c, d where polarization and electric field vectors along the core were plotted from the full 2D map of the polarization and electric field vectors.

The change in polarization always aligns with the external field—that is, $\partial P/\partial E_{\mathrm{external}}$ or the conventional susceptibility is always positive, even locally. This is shown in Extended Data Fig. 5b. The local susceptibility is always positive even in the regions where the permittivity itself is negative. Regions of negative permittivity arise where the susceptibility becomes very large, that is, where the material becomes highly polarizable. This is also discussed in Methods section 'Estimation of the permittivity', where we show that the permittivity estimated from the experimental data becomes negative only when the polarizability is very high.

An important aspect of our work is the simultaneous mapping of both the polarity[18] and the electric field[23] inside the polarization vortices. This is what makes it possible to estimate the local energy density and therefore the local permittivity. Mapping out the local polarization[26–29] alone would not be enough to probe local permittivity. Vortices allow domain walls to form, and domain walls allow polarization to be suppressed—and it is in regions of suppressed polarization that negative capacitance emerges. Thus vortices lead to the emergence of negative capacitance. A key insight that can be gained from this work is that, in a multi-domain system, the negative capacitance emerges in the domain walls[14], and it should be possible to control its strength by engineering the energetics of the system that increase or decrease the size of the domain wall. In this vein, the superlattice structure that we used is one example; but bilayer, trilayer or any other combination of ferroelectric–dielectric is equally applicable. A recent theoretical study[30] has shown how negative capacitance may be stabilized in the nanodomains in a ferroelectric thin film. In the same context, systems with mixed Bloch–Néel domain walls[31] could be relevant. Further work should also investigate improper ferroelectrics[32] where polarization is not the order parameter.

In summary, we report the observation of steady-state arrays of negative capacitance in epitaxial superlattices composed of ferroelectric $PbTiO_3$ and non-ferroelectric $SrTiO_3$. The polarization in the $PbTiO_3$ layer accommodates the competition between elastic and electrostatic energies by forming arrays of clockwise and anticlockwise vortex-like structures. The core of such vortices displays regions of suppressed polarization and larger energy densities where the total change in the internal field dominates over the change in the external field[33], making the curvature $\partial^2 G/\partial D^2$ negative. The fact that two different theoretical models can reproduce the experimental observation indicates that such stabilization in the 'forbidden' region of the thermodynamic landscape should be amenable to predictive material design. Last, we note that the superlattice forms a periodic array of negative and positive capacitance states, pointing to the possibility of new types of metamaterial.

Online content

Any methods, additional references, Nature Research reporting summaries, source data, statements of data availability and associated accession codes are available at https://doi.org/10.1038/s41586-018-0855-y.

Received: 29 May 2018; Accepted: 16 October 2018;
Published online 14 January 2019.

1. Lines, M. E. & Glass, A. M. *Principles and Applications of Ferroelectrics and Related Materials* (Oxford Univ. Press, Oxford, 2001).
2. Salahuddin, S. & Datta, S. Use of negative capacitance to provide voltage amplification for low power nanoscale devices. *Nano Lett.* **8**, 405–410 (2008).
3. Salahuddin, S. & Datta, S. Can the subthreshold swing in a classical FET be lowered below 60 mV/decade? In *2008 IEEE International Electron Devices Meeting (IEDM)* 1–4 (2008).
4. Khan, A. I. et al. Experimental evidence of ferroelectric negative capacitance in nanoscale heterostructures. *Appl. Phys. Lett.* **99**, 113501 (2011).
5. Theis, T. N. & Solomon, P. M. It's time to reinvent the transistor! *Science* **327**, 1600–1601 (2010).
6. Gao, W. et al. Room-temperature negative capacitance in a ferroelectric–dielectric superlattice heterostructure. *Nano Lett.* **14**, 5814–5819 (2014).
7. Appleby, D. J. et al. Experimental observation of negative capacitance in ferroelectrics at room temperature. *Nano Lett.* **14**, 3864–3868 (2014).
8. Rusu, A., Salvatore, G., Jiménez, D. & Ionescu, A. M. Metal-ferroelectric-meta-oxide-semiconductor field effect transistor with sub-60mv/decade subthreshold swing and internal voltage amplification. In *2010 IEEE International Electron Devices Meeting (IEDM)* 16.3.1–16.3.4 (2010).
9. Li, K.-S. et al. Sub-60mv-swing negative-capacitance finFET without hysteresis. In *2015 IEEE International Electron Devices Meeting (IEDM)* 22.6.1–22.6.4 (2015).
10. Krivokapic, Z. et al. 14nm ferroelectric finFET technology with steep subthreshold slope for ultra low power applications. In *2017 IEEE International Electron Devices Meeting (IEDM)* 15.1.1–15.1.4 (2017).
11. Jo, J. & Shin, C. Negative capacitance field effect transistor with hysteresis-free sub-60-mv/decade switching. *IEEE Electron Device Lett.* **37**, 245–248 (2016).
12. Kwon, D. et al. Improved subthreshold swing and short channel effect in FDSOI n-channel negative capacitance field effect transistors. *IEEE Electron Device Lett.* **39**, 300–303 (2018).
13. Khan, A. I. et al. Negative capacitance in a ferroelectric capacitor. *Nat. Mater.* **14**, 182–186 (2015).
14. Zubko, P. et al. Negative capacitance in multidomain ferroelectric superlattices. *Nature* **534**, 524–528 (2016).
15. Cano, A. & Jiménez, D. Multidomain ferroelectricity as a limiting factor for voltage amplification in ferroelectric field-effect transistors. *Appl. Phys. Lett.* **97**, 133509 (2010).
16. Karpov, D. et al. Three-dimensional imaging of vortex structure in a ferroelectric nanoparticle driven by an electric field. *Nat. Commun.* **8**, 280 (2017).
17. Wang, J., Kamlah, M., Zhang, T.-Y., Li, Y. & Chen, L.-Q. Size-dependent polarization distribution in ferroelectric nanostructures: phase field simulations. *Appl. Phys. Lett.* **92**, 162905 (2008).
18. Yadav, A. K. et al. Observation of polar vortices in oxide superlattices. *Nature* **530**, 198–201 (2016); corrigendum **534**, 138 (2016).
19. Hong, Z. et al. Stability of polar vortex lattice in ferroelectric superlattices. *Nano Lett.* **17**, 2246–2252 (2017).
20. Damodaran, A. R. et al. Phase coexistence and electric-field control of toroidal order in oxide superlattices. *Nat. Mater.* **16**, 1003–1009 (2017).
21. Urban, K. W. Studying atomic structures by aberration-corrected transmission electron microscopy. *Science* **321**, 506 (2008).
22. Jia, C.-L. et al. Unit-cell scale mapping of ferroelectricity and tetragonality in epitaxial ultrathin ferroelectric films. *Nat. Mater.* **6**, 64–69 (2007).
23. Nguyen, K. X. et al. Reconstruction of polarization vortices by diffraction mapping of ferroelectric $PbTiO_3/SrTiO_3$ superlattice using a high dynamic range pixelated detector. *Microsc. Microanal.* **22**, 472–473 (2016).
24. Nelson, C. T. et al. Spontaneous vortex nanodomain arrays at ferroelectric heterointerfaces. *Nano Lett.* **11**, 828–834 (2011).
25. Watanabe, Y. in *Ferroelectric Thin Films: Basic Properties and Device Physics for Memory Applications* (eds Okuyama, M. & Ishibashi, Y.) 177–199 (Springer, Berlin, 2005).
26. Qi, Y. et al. Coexistence of ferroelectric vortex domains and charged domain walls in epitaxial $BiFeO_3$ film on $(110)_O$ $GdScO_3$ substrate. *J. Appl. Phys.* **111**, 104117 (2012).
27. Lee, M. H. et al. Hidden antipolar order parameter and entangled Néel-type charged domain walls in hybrid improper ferroelectrics. *Phys. Rev. Lett.* **119**, 157601 (2017).
28. Zhang, Q. et al. Direct observation of multiferroic vortex domains in $YMnO_3$. *Sci. Rep.* **3**, 2741 (2013).
29. Gruverman, A. et al. Vortex ferroelectric domains. *J. Phys. Condens. Matter* **20**, 342201 (2008).
30. Sluka, T., Mokry, P. & Setter, N. Static negative capacitance of a ferroelectric nano-domain nucleus. *Appl. Phys. Lett.* **111**, 152902 (2017).
31. Lee, D. et al. Mixed Bloch-Néel-Ising character of 180 ferroelectric domain walls. *Phys. Rev. B* **80**, 060102 (2009).
32. Bousquet, E. et al. Improper ferroelectricity in perovskite oxide artificial superlattices. *Nature* **452**, 732 (2008).
33. Chang, S. C., Avci, U. E., Nikonov, D. E. & Young, I. A. A thermodynamic perspective of negative-capacitance field-effect transistors. *IEEE J. Explor. Solid-State Comput. Devices Circuits* **3**, 56–64 (2017).

Acknowledgements This work was supported in part by the AFOSR YIP programme, LEAST (one of the SRC/DARPA supported centres within the STARNET initiative), ASCENT (one of the SRC/DARPA supported centres within the JUMP initiative), and the Berkeley Center for Negative Capacitance Transistors and the Multicampus Research Programs and Initiatives (MRPI) of the University of California. Electron microscopy experiments and equipment were supported by the Cornell Center for Materials Research, through the National Science Foundation MRSEC programme, award DMR 1719875. The work at Penn State was supported by the US Department of Energy, Office of Basic Energy Sciences, Division of Materials Sciences and Engineering under award FG02-07ER46417. Z.J.H. acknowledges support from NSF-MRSEC grant number DMR-1420620 and NSF-MWN grant number DMR-1210588. R.R. and S.D. acknowledge support from the Gordon and Betty Moore Foundation's EPiQS Initiative, under grant GBMF5307. R.R. also acknowledges funding from the Army Research Office. J.I. acknowledges support from the Luxembourg National Research Fund under grant C15/MS/10458889 NEWALLS. P.G.-F. and J.J. acknowledge financial support from the Spanish Ministry of Economy and Competitiveness through grant number FIS2015-64886-C5-2-P, and P.G.-F. acknowledges support from Ramón y Cajal grant no. RyC-2013-12515.

Reviewer information *Nature* thanks D. Jiménez, J. Rondinelli and the other anonymous reviewer(s) for their contribution to the peer review of this work.

Author contributions A.K.Y., K.X.N., D.A.M., R.R. and S.S. designed the research. A.K.Y. performed synthesis and characterization of superlattice films. K.X.N. performed polarization and electric field measurements on superlattice films using EMPAD-STEM. C.T.N. performed atomic-resolution polar displacement mapping on superlattice films using STEM. Z.H. and L.-Q.C. performed phase-field calculations for these superlattice structures. P.G.-F., P.A.-P., J.I. and J.J. performed second-principles calculations for these superlattice structures. D.K., S.C., S.D. and B.P. performed current–voltage measurements. A.K.Y., S.S., C.H., R.R., K.X.N., C.T.N., A.I.K., Z.H., P.G.-F., P.A.-P., J.J., L.-Q.C., D.A.M. and J.I. discussed results and co-wrote the manuscript. S.S. performed the overall supervision of the work. All authors contributed to the discussions and manuscript preparation.

Competing interests The authors declare no competing interests.

Additional information
Extended data is available for this paper at https://doi.org/10.1038/s41586-018-0855-y.
Reprints and permissions information is available at http://www.nature.com/reprints.
Correspondence and requests for materials should be addressed to S.S.
Publisher's note: Springer Nature remains neutral with regard to jurisdictional claims in published maps and institutional affiliations.

METHODS

Synthesis. A pulsed laser deposition (PLD) method was used to synthesize thin films of superlattice structures of strontium titanate ($SrTiO_3$) and lead titanate ($PbTiO_3$) on a single crystalline substrate ($DyScO_3(001)_{pc}$). The PLD growth technique was employed in combination with the reflection high energy electron diffraction (RHEED) technique to monitor the growth of oxides in situ, and achieve desired thickness of respective layers in the superlattice structure. The growth conditions for different oxides were optimized independently to achieve a persistent layer-by-layer (Frank-van de Merwe) growth mode up to a film thickness of 100 nm or more. To achieve the layer-by-layer growth mode of $SrTiO_3$, growth temperature was set to 630 °C with an oxygen pressure of 100 mtorr and a laser fluence of 1.5 J cm^{-2} on the stoichiometric $SrTiO_3$ target[18]. For the deposition of stoichiometric $PbTiO_3$ film, we used a 20% lead-excess target, that is, $Pb_{1.2}TiO_3$, to achieve both layer-by-layer growth mode and stoichiometric transfer of $PbTiO_3$ onto the substrate[18]. This was achieved at a growth temperature of 630 °C, an oxygen pressure of 100 mtorr and a laser fluence of 1.5 J cm^{-2} (ref. [1]). At these optimized growth conditions, RHEED was used as an in situ technique to monitor the growth of superlattice structures along the $[100]_{pc}$ in-plane direction of the $[001]_{pc}$-oriented $DyScO_3$ substrate[1]. All superlattice structures $(SrTiO_3)_n/(PbTiO_3)_n$ were grown on a 5 nm $SrRuO_3$-buffered $DyScO_3(001)_{pc}$ substrate. The growth conditions of the $SrRuO_3$ buffer layer were optimized as a set temperature of 700 °C, an oxygen pressure of 50 mtorr, and a laser fluence of 1.5 J cm^{-1} (refs [2,18]). All oxide films were deposited at a laser output frequency of 10 Hz. After deposition, films were cooled down to room temperature at an oxygen pressure of 50 torr to ensure full oxidation of oxide films.

EMPAD. All superlattice films were characterization by various ex situ characterization techniques, such as laboratory-based X-ray diffraction, synchrotron-based X-ray diffraction, atomic-resolution scanning transmission electron microscopy, and so on, which are discussed in our previous work[18,20]. For this study, we perform diffraction imaging in scanning transmission electron microscopy (STEM) mode using a 200 keV uncorrected FEI Tecnai F20 and an electron microscopy pixel array detector (EMPAD)[23]. Here, the EMPAD acquires the full convergent beam electron diffraction (CBED) pattern at each scan position such that our total data set is four-dimensional: x, y, k_x and k_y, where x and y are the scan dimensions and k_x and k_y are the dimensions of our CBED pattern.

To reconstruct the macroscale electric and polarization fields from our specimen, we realized that the average electric field $E(r_0)$ (ref. [34]) is equal to the average field over the volume of the crystal cell V_c that contains the lattice point r_0; see equation (1). Therefore, instead of having an atomic-sized probe as in traditional STEM imaging, we need a bigger probe so that we can average over the unit cell. Here, we are no longer restricted to be in a small field of view where every atom must be resolved to be counted.

To perform the experiment, we prefer a 3 mrad semi-convergence angle to produce a 7 Å beam (Extended Data Fig. 1a) such that we can get the macroscale electric and polarization fields. From these, the electric field can be extracted with the (000) spot (Extended Data Fig. 1c) by calculating the probability current flow ($\langle \boldsymbol{p} \rangle$):

$$\langle \boldsymbol{p} \rangle = \int \psi(p)^* \hat{\boldsymbol{p}} \psi(p) \mathrm{d}\boldsymbol{p} = \int \hat{\boldsymbol{p}} \, |\psi(p)|^2 \, \mathrm{d}p = \int \hat{\boldsymbol{p}} I \mathrm{d}p$$

where ψ is the exit wavefunction after scattering. Probability current flow $\langle \boldsymbol{p} \rangle$ can then be related back to Erhenfest's theorem and the Lorentz force law by

$$\frac{\mathrm{d}\langle \boldsymbol{p} \rangle}{\mathrm{d}t} = \langle [H, \boldsymbol{p}] \rangle = \langle q\boldsymbol{E} + \boldsymbol{v} \times \boldsymbol{B} \rangle$$

such that the electric field can be extracted from the shift in the first moment of the probability current flow.

When a long-range electric field is observed, the electron field signal shifts the entire CBED pattern. We specifically choose the (000) spot to reconstruct the electric field (Extended Data Fig. 1c) because there are no polarity effects for this beam. In addition, we observed that our specimen is relatively flat and thickness effects do not dominate our signal. To extract polarity, probability current flow ($\langle \boldsymbol{p} \rangle$) measurements are made for conjugate disk pairs (200)/($\bar{2}00$) and (020)/($0\bar{2}0$) to calculate the x and z component of polarity, respectively (Extended Data Fig. 1c, d). Here, Friedel's rule tells us that conjugated disk pairs should have the same intensities by symmetry; however, if an effect such as polarity, tilt or thickness persists, an asymmetry in intensities will occur between our conjugated disk pairs. Here again, we show tilt and thickness effects do not dominate our signal. Thus, we can extract the polarity field, P_x and P_z (Extended Data Fig. 2c, d), which essentially stems from the presence of a spatially varying polarization field within the sample.

Phase-field simulations. Phase-field simulations are conducted to investigate stabilization of negative capacitance in clockwise–anticlockwise vortex structures. More specifically, we have performed phase-field simulations to understand the polarization distribution and calculate the small-field local dielectric constants for $n \times n$ $PbTiO_3/SrTiO_3$ superlattices on a (110) oriented $DyScO_3$ substrate (where n represents the number of unit cells of respective materials, that is, $PbTiO_3$ or $SrTiO_3$). The spontaneous polarization vector ($\boldsymbol{P}$) is chosen as the order parameter, which is obtained by minimizing the total free energy:

$$\frac{\partial P_i}{\partial t} = -L\frac{\delta F}{\delta P_i} \quad (i = 1, 2, 3)$$

The total free energy (F) is composed of bulk Landau chemical, elastic, electric and polarization gradient energies:

$$F = \int (f_{\mathrm{bulk}} + f_{\mathrm{elastic}} + f_{\mathrm{electric}} + f_{\mathrm{gradient}}) \mathrm{d}V$$

The procedures used to obtain the free-energy densities are described in detail in previous reports[18,19,35,36]. A 3D mesh of 200 × 200 × 250 grids is used, with each grid representing 0.4 nm. Periodic boundary conditions are applied on the in-plane dimensions, while the superposition method is used in the thickness direction[37]. The elastic boundary condition is applied where the out-of-plane stress at the top surface of the film is zero while the displacement at the bottom of the substrate sufficiently far away from the substrate/film interface is set as zero. A short-circuit electric boundary condition is set where the electric potential is zero on the bottom electrode and the applied electric potential is at the top of the film. Random noise is used as the initial nuclei with a small magnitude (<0.0005 C m^{-2}), and then relaxed to equilibrium. In order to calculate the local dielectric constant, we perturb the structure using small capacitor bias (0.01 V) from the film top. The local dielectric constant can be calculated by the change in local electric displacement ($\boldsymbol{D}$) divided by the change in local electric field ($\boldsymbol{E}$):

$$\epsilon_{ij} = \frac{\Delta D_i}{\epsilon_0 \Delta E_j} \quad (i = 1, 2, 3; j = 1, 2, 3)$$

$$D_i = P_i + \epsilon_0 k_{ij} E_j$$

where ϵ_0 and k_{ij} are the permittivity of vacuum and background dielectric constants[38–40], respectively. The isotropic background dielectric constants[19] are set as $k_{11} = k_{22} = k_{33} = 40$. The local electric field ($\boldsymbol{E}$) is obtained by solving Poisson's equation:

$$k_{ij}\frac{\partial^2 \phi}{\partial x_i \partial x_j} = \frac{\partial P_i}{\epsilon_0 \partial x_i}$$

$$E_i = \frac{\partial \phi}{\partial x_i}$$

Extended Data Fig. 3 shows the calculated polarization and electric field vector maps. Also shown is the line cut that was used to plot P_z and E_z in Fig. 4a, c. Note that the vortex structures are repeated in the x direction. Reading from left to right, the polarization changes from up to down in a clockwise vortex along the line. On the other hand, the polarization changes from down to up in the anticlockwise vortex. In Fig. 4a, c, we plot the polarization variation corresponding to the experimentally observed vortex structure as shown in Fig. 3a. The same thing was done for the second-principles calculation, as discussed in the next section.

Second-principles calculations. For the second-principles simulations, we use the methods implemented in the SCALE-UP code[41,42], and the model for $PbTiO_3/SrTiO_3$ superlattices originally introduced in ref. [14] and slightly revised in ref. [43]. In classical electrodynamics[44], the dielectric tensor of a medium is defined as the tensor of rank two that relates, to linear order, the electric displacement field $\boldsymbol{D}$ and the averaged macroscale electric field $\boldsymbol{E}$ within the material.

If we consider the whole $PbTiO_3/SrTiO_3$ superlattice as a continuum medium, forgetting for a while all its details at the atomic level, we can define the total dielectric tensor of the system as

$$\epsilon^{\mathrm{tot}}_{\alpha\beta} = \frac{1}{\epsilon_0}\frac{\mathrm{d}D_\alpha}{\mathrm{d}E^{\mathrm{int}}_\beta}$$

where α and β refer to Cartesian directions in the system and ϵ_0 is the vacuum permittivity. From this definition, we see that the accessible physical quantity that can be experimentally measured is the change in the electric displacement, that is, the response of the medium, with respect to the applied electric field.

We define the local dielectric constant as the variation in the global (averaged over the whole superlattice) macroscale displacement vector with respect to the local electric field

$$\epsilon_{\alpha\beta}(x,z)=\frac{1}{\epsilon_0}\frac{\mathrm{d}D_\alpha}{\mathrm{d}E_\beta} \tag{2}$$

where x and z refer to the coordinates of a given position in the material in real space and the derivative is taken with respect to local electric field at that point. We assume from here on that the whole system is homogeneous in the third Cartesian direction parallel to the axis of the vortices (y), so we drop it from the discussion. The local electric field $\boldsymbol{E}(x,z)$ is the sum of the external contributions plus all the possible internal fields generated by the non-trivial polarization field. In our simulations the global electric displacement is taken as a single control parameter. Assuming that we work with a capacitor under open-circuit boundary conditions[45], and the surfaces of the superlattices are insulating, then the normal component of the electric displacement (along the z direction) is preserved at the vacuum/material interface[46]. Because in vacuum $D_z=\epsilon_0 E_z^{\mathrm{ext}}$, the normal component of $\boldsymbol{D}$ can be monitored by the external electric field. Focusing on the diagonal component of the dielectric tensor along z, the physical meaning of equation (2) is more evident if we take its inverse:

$$\frac{1}{\epsilon_{zz}(x,z)}=\epsilon_0\frac{\mathrm{d}E_z(x,z)}{\mathrm{d}D_z}=\frac{\mathrm{d}E_z(x,z)}{\mathrm{d}E_z^{\mathrm{ext}}} \tag{3}$$

This definition, which is the most suitable for computation of the local dielectric constant from second principles (see below), sets the inverse of the dielectric constant to be a measurement of the change in the local electric field with the variation of the electrical boundary conditions (the external field).

The local electric field, the basic ingredient required in equation (3), can be easily computed from a finite difference derivative of the electrostatic potential, routinely available from a second-principles simulation[42]. The (x,z) plane in the simulation box of our $SrTiO_3/PbTiO_3$ superlattices is discretized in three staggered regular grids (Extended Data Fig. 4), whose points are indexed with two integer numbers (i,j). The discretization of the fundamental relation between the electric field and the electrostatic potential, $\boldsymbol{E}=-\boldsymbol{\nabla}V$, along the z direction reads

$$-\Delta z E_z^{ij}=V_{ij+1}-V_{ij} \tag{4}$$

where Δz is the distance between consecutive points of the grid, as shown in Extended Data Fig. 5.

To get the variation in the displacement field, as required by equation (3), we carry out second-principles simulations, assuming that the system is subject to two different external fields, that is, to two different electric displacements $\boldsymbol{D}^{(1)}$ and $\boldsymbol{D}^{(2)}$. We use equation (4) to trivially obtain

$$-\Delta z\delta E_z^{ij}=\delta V_{ij+1}-\delta V_{ij}$$

where magnitudes such as δV_{ij} are defined as

$$\delta V_{ij}=V_{ij}^{(2)}-V_{ij}^{(1)}$$

Using the definition of the inverse of the local dielectric constant, equation (3), we get

$$-\Delta z\sum_\alpha\frac{1}{\epsilon_0}\frac{1}{\epsilon_{\alpha z}^{ij}}\delta D_\alpha=\delta V_{ij+1}-\delta V_{ij} \tag{5}$$

Taking the two situations to have vertical displacement vectors in opposite directions,

$$\boldsymbol{D}^{(1)}=-D_0\boldsymbol{u}_z$$
$$\boldsymbol{D}^{(2)}=+D_0\boldsymbol{u}_z$$
$$\delta\boldsymbol{D}=2D_0\boldsymbol{u}_z$$

using equation (5) we obtain

$$\frac{1}{\epsilon_{zz}^{ij}}=-\epsilon_0\frac{\delta V_{ij+1}-\delta V_{ij}}{2D_0\Delta z}$$

Extended Data Fig. 5a shows the inverse of the dielectric constant along z, $(\epsilon_{zz}^{ij})^{-1}$, computed at every point in the (x,z) plane. The green dashed line in Extended Data Fig. 5a shows the line cut that is used to plot Fig. 4. The negative permittivity regions can be clearly seen in the centre of the vortices and also at the interface between the ferroelectric and dielectric. Finally, Extended Data Fig. 5b shows the susceptibility. The local susceptibility becomes very large in the cores where the permittivity is also negative. We observe that the regions with a negative dielectric constant are located: (i) at vortex cores (where the polarization vectors are suppressed), and (ii) at the interfaces between the dielectric $SrTiO_3$ and the ferroelectric $PbTiO_3$. Those are precisely also the regions where the higher susceptibility is observed. Further, the local polarizations at the interfaces, which in the absence of any external field tend to rotate in order to close the polarization flux, will suffer the largest changes to align with the applied field. Conversely, the centres of the domains are essentially rigid objects where only small changes of polarization (electric susceptibilities) are observed. Those are the regions that display large and positive values of the dielectric constant.

The transition between the local microscale values of the dielectric constant and the macroscale dielectric constant for the superlattice as a whole can be calculated by taking the derivative of the average of the internal electric field along z throughout the whole superlattice $\langle E\rangle$ with respect the external electric field. Within our open-circuit electrostatic boundary conditions, $(\epsilon_{zz}^{\mathrm{tot}})^{-1}=\mathrm{d}\langle E\rangle/\mathrm{d}E^{\mathrm{ext}}$.

Finally, to calculate the local energy from second principles, we notice that in our expressions for the model potentials[41] the energy is written as a function of arbitrary atomic distortions by means of a Taylor expansion around a suitable chosen reference configuration. In order to fulfil the acoustic sum rule, it is convenient to write all the energy contributions as linear combinations of products of displacement differences and/or strains to different orders.

We divide the energy of each of the terms in the linear expansion into atomic components using the following recipe: (i) we take a term in the sum and divide its total contribution by its order (the number of factors in the product), so we assign a given amount of energy to each factor. (ii) Then we divide each of these factor energies into atomic pieces following the rule that if the factor is a strain coordinate then we divide the contribution among all the atoms in the system, and if the factor is a difference of two atomic coordinates, then we divide that contribution equally between the two atoms participating in the difference.

Once we have split the total energy into atomic pieces, we compute the energy contribution of each of the perovskite cells by adding the atomic energy contributions of the atoms in that cell. Finally, we add the electrostatic energy integrating the square of the electric field within a unit cell. The local energy density obtained following this scheme is plotted in Extended Data Fig. 6. The most important conclusions that can be drawn from this figure are: (i) within the $PbTiO_3$ domains, the energy is much lower than in the reference centrosymmetric phase owing to the local ferroelectric distortions; (ii) the domain walls store energy, as represented by the paler colour with respect that observed at the middle of the domains; and (iii) within the dielectric $SrTiO_3$ region the local energy is close to the reference energy, suggesting that once we are in the decoupled regime, $SrTiO_3$ behaves like a separation barrier between the ferroelectric layers of the superlattice.

Extended Data Fig. 6 corresponds well with the intuitive double-well picture shown in Fig. 1 that shows that it is the higher energy regions that lead to negative permittivity while the lower energy wells have positive permittivity.

Estimation of the free energy (G). Experimentally measured E_z and P_z (as shown in Fig. 3c) allow us to plot E_z as a function of P_z, obtaining essentially the same result, within experimental resolution, as we move from one core to another. As mentioned in the main text, this is an approximation to the constitutive equation of our $PbTiO_3$ layers, which are in a complex multidomain ferroelectric state; yet, as a working hypothesis, we assume this empirical result to contain relevant information about the internal energy density and therefore the dielectric response[45]. We find the displacement D_z as

$$D_z=\epsilon_0E_z+P_z$$

Extended Data Fig. 7a shows E_z as a function of D_z. From this relationship the free energy G can be estimated as

$$G=\int E_z\mathrm{d}D_z$$

Note that taking only z components suffices as the x component of the polarization is negligible along the line where P_z and E_z are plotted. Extended Data Fig. 7b shows G as a function of D_z, in which the regions where the curvature $\partial^2G/\partial D^2$ is negative are clear. We further correlate D_z to the corresponding local positions in the real space where they occur. Doing that allows us to estimate a local variation of G, which is plotted in Fig. 3d. We find that the regions at and near the core correspond to higher energy densities and negative curvature ($\partial^2G/\partial D^2<0$). This corresponds very well with second-principles calculations, as shown in Extended Data Fig. 6.

Estimation of the permittivity. It is important to note that in stationary conditions, a microscale dielectric susceptibility tensor that relates the local electric field at a given point and the induced local polarization at another point can be defined[47]. As described in Methods section 'EMPAD', during the EMPAD measurements, an average is taken over the unit cell to measure the local electric field. As a

result, as far as the measured field is concerned, short-range non-local interactions are averaged out and a local permittivity can be defined following

$$\tilde{\epsilon}_{\alpha\beta}(x,z) = 1 + \tilde{\chi}_{\alpha\beta}(x,z) \tag{6}$$

where the local susceptibility, $\tilde{\chi}_{\alpha\beta}(x,z)$, is computed as the derivative of the local polarization with respect to the local electric field. This is the most accessible estimation of the local dielectric constant from the experimental point of view within this work, since the local polarization and the local electric fields are measured directly and independently with the EMPAD microscope.

Starting from equation (6), and restricting ourselves to the diagonal component of the local dielectric constant along z, we write

$$\tilde{\epsilon}_{zz}(x,z) = 1 + \frac{1}{\epsilon_0}\frac{\mathrm{d}P_z(x,z)}{\mathrm{d}E_z(x,z)} \tag{7}$$

To estimate permittivity we first confine our attention to the line A–B in Fig. 2a, which is the farthest from the interfaces. We first look into the quantity $\mathrm{d}E_z$, which is the change in the total field (that includes the external field and all internal fields) due to the application of a small external voltage ($\mathrm{d}E_z = \mathrm{d}E_{\mathrm{ext}} + \mathrm{d}E_{\mathrm{int}}$). Because $\mathrm{d}P/\mathrm{d}E_{\mathrm{ext}}$ is always positive, a negative permittivity appears only when $\mathrm{d}E_z < 0$ even though $\mathrm{d}E_{\mathrm{ext}} > 0$. In other words, for negative capacitance we need

$$\begin{aligned} &\Delta E_z = \Delta E_{\mathrm{ext}} + \Delta E_{\mathrm{int}} < 0 \\ \Longrightarrow\ &\frac{\Delta E_{\mathrm{int}}}{\Delta E_{\mathrm{ext}}} < -1 \\ \Longrightarrow\ &\frac{\partial E_{\mathrm{int}}}{\partial P_z}\frac{\partial P_z}{\partial E_{\mathrm{ext}}} < -1 \end{aligned} \tag{8}$$

As discussed in the previous section, the quantity $\partial E_{\mathrm{int}}/\partial P_z$ can be estimated in our experiments by introducing an approximate constitutive relationship between local polarization and field. Note that the small change in the external field (which in this case is a constant field in the z direction) is not expected to lead to any abrupt change to the relation between P_z and E_z (ref. [45]). Also, equation (8) is fully compatible with equation (3) used in the second-principles calculations taking into account that the derivative in equation (3) is with respect to the full internal field E_z.

In the region near the core we can also estimate the value of $\partial P_z/\partial E_{z,\mathrm{ext}} = \epsilon_0\chi_{zz,\mathrm{ext}}$. This region is analogous to an isolated ferroelectric at elevated temperature where its polarization is suppressed substantially and $\chi_{zz,\mathrm{ext}}$ is enhanced substantially. Numerous experiments have measured $\chi_{zz,\mathrm{ext}}$ $PbTiO_3$ films close to the transition temperature, where polarization goes down to similar values as we see near the core. The values[48–50] vary from 2,000 to 8,000, depending on thickness, method of synthesis, frequency of measurement, and so on. Nonetheless, over this entire range, the ratio on the left-hand side of the final equation in equation (8) has a value between −5 and −20, thus easily satisfying the condition. Therefore, the change in the total field is estimated to be negative ($\mathrm{d}E_z < 0$).

The above analysis also shows that $|\Delta E_{\mathrm{int}}| \gg |\Delta E_{\mathrm{ext}}|$ near the core. Thus, at and around the core region, we can estimate the permittivity from equation (7) as shown in Extended Data Fig. 8. The regions near the core are found to show negative permittivity. This corresponds very well with the phase-field and second-principles calculations as shown in Fig. 4b, d. Such a good correspondence suggests that the approximations on which we base our empirical analysis capture correctly the essential features of the system's response. Further theoretical investigations will be required to investigate the applicability of such approximations in a generic manner.

Macroscale capacitance measurement. Macroscale demonstration of stabilization in the negative capacitance state manifests itself in the enhancement of capacitance of the superlattice compared to its constituent dielectric ($SrTiO_3$) capacitance[4]. Extended Data Fig. 9 shows the measurement of permittivity (ϵ_{SL}) of the superlattice sample (100 nm thick) with respect to the permittivity (ϵ_{STO}) of its constituent dielectric $SrTiO_3$ (STO; combined thickness adding all the layers is 50 nm). If the superlattice has to have a larger capacitance than the constituent $SrTiO_3$ capacitance ($C_{\mathrm{SL}} > C_{\mathrm{STO}}$), then $\epsilon_{\mathrm{SL}} > \epsilon_{\mathrm{STO}}(t_{\mathrm{SL}}/t_{\mathrm{STO}})$, which leads to

$$\epsilon_{\mathrm{SL}} > 2\epsilon_{\mathrm{STO}}$$

The factor of 2 results from the fact that the number of cycles used for $PbTiO_3$ and $SrTiO_3$ in the superlattice is the same. In Extended Data Fig. 9, this threshold of $2\epsilon_{\mathrm{STO}}$ is shown with a dashed line. The permittivity of the superlattice is 3.7 times larger than this threshold, clearly showing capacitance enhancement and therefore the stabilization of $PbTiO_3$ in a state of negative capacitance.

Data availability

All data supporting the findings of this study are available within the paper.

34. Kittel, C. *Introduction to Solid State Physics* (Wiley, Hoboken, 1966).
35. Chen, L.-Q. Phase-field method of phase transitions/domain structures in ferroelectric thin films: a review. *J. Am. Ceram. Soc.* **91**, 1835–1844 (2008).
36. Li, Y. L., Hu, S. Y., Liu, Z. K. & Chen, L. Q. Effect of substrate constraint on the stability and evolution of ferroelectric domain structures in thin films. *Acta Mater.* **50**, 395–411 (2002).
37. Chen, L. Q. & Shen, J. Applications of semi-implicit Fourier-spectral method to phase field equations. *Comput. Phys. Commun.* **108**, 147–158 (1998).
38. Tagantsev, A. K. Landau expansion for ferroelectrics: which variable to use? *Ferroelectrics* **375**, 19–27 (2008).
39. Yue, Z. & Woo, C. H. Giant piezoelectric resistance in ferroelectric tunnel junctions. *Nanotechnology* **20**, 075401 (2009).
40. Tagantsev, A. K. & Gerra, G. Interface-induced phenomena in polarization response of ferroelectric thin films. *J. Appl. Phys.* **100**, 051607 (2006).
41. Wojdeł, J. C., Hermet, P., Ljunberg, M. P., Ghosez, Ph. & Íñiguez, J. First-principles model potentials for lattice-dynamical studies: general methodology and example of application to ferroic perovskite oxides. *J. Phys. Condens. Matter* **25**, 305401 (2013).
42. García-Fernández, P., Wojdeł, J. C., Íñiguez, J. & Junquera, J. Second-principles method including electron and lattice degrees of freedom. *Phys. Rev. B* **93**, 195137 (2016).
43. Shafer, P. et al. Emergent chirality in the electric polarization texture of titanate superlattices. *Proc. Natl Acad. Sci. USA* **115**, 915–920 (2018).
44. Landau, L. D. & Lifshitz, E. M. *Electrodynamics of Continuous Media* (Pergamon, Oxford, 1989).
45. Stengel, M., Spaldin, N. A. & Vanderbilt, D. Electric displacement as the fundamental variable in electronic-structure calculations. *Nat. Phys.* **5**, 304–308 (2009).
46. Stengel, M., Vanderbilt, D. & Spaldin, N. A. First-principles modeling of ferroelectric capacitors via constrained displacement field calculations. *Phys. Rev. B* **80**, 224110 (2009).
47. Giustino, F. & Pasquarello, A. Theory of atomic-scale dielectric permittivity at insulator interfaces. *Phys. Rev. B* **71**, 144104 (2005).
48. Bhide, V. G., Hegde, M. S. & Deshmukh, K. G. Ferroelectric properties of lead titanate. *J. Am. Ceram. Soc.* **51**, 565–568 (1968).
49. Chaudhari, V. A. & Bichile, G. K. Synthesis, structural, and electrical properties of pure $PbTiO_3$ ferroelectric ceramics. *Smart Mater. Res.* **2013**, 147524 (2013).
50. Sidorkin, S. et al. Dispersion of dielectric permittivity in thin ferroelectric lead titanate films. *Solid State Phenom.* **115**, 233-238 (2006).

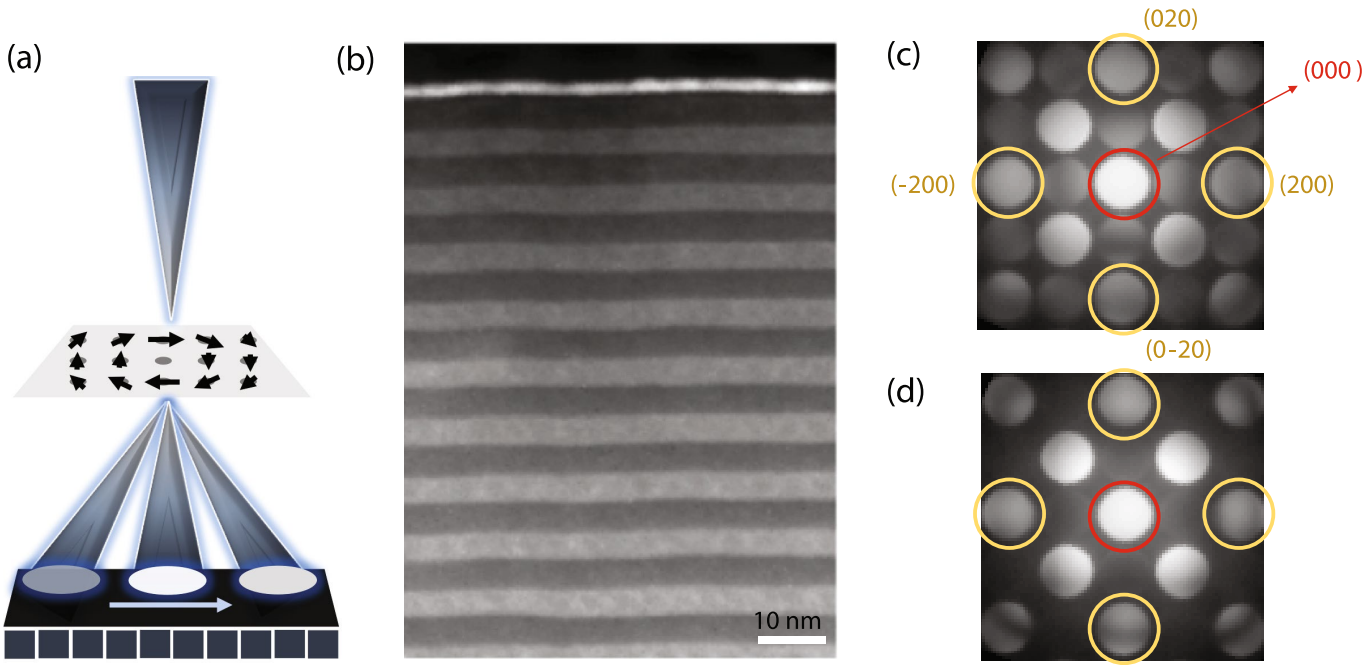

Extended Data Fig. 1 | Electron spectrometry of the superlattice. **a**, Schematic of the electron microscopy pixel array detector (EMPAD) placed in the diffraction plane to record the full angular scattering distribution from an electron beam focused onto a sample. **b**, ADF image of the $(PbTiO_3)_{12}/(SrTiO_3)_{12}$ superlattice along the $[010]_{pc}$ zone axis. **c**, **d**, CBED pattern from the $PbTiO_3$ layer (**c**) and from the $SrTiO_3$ layer (**d**).

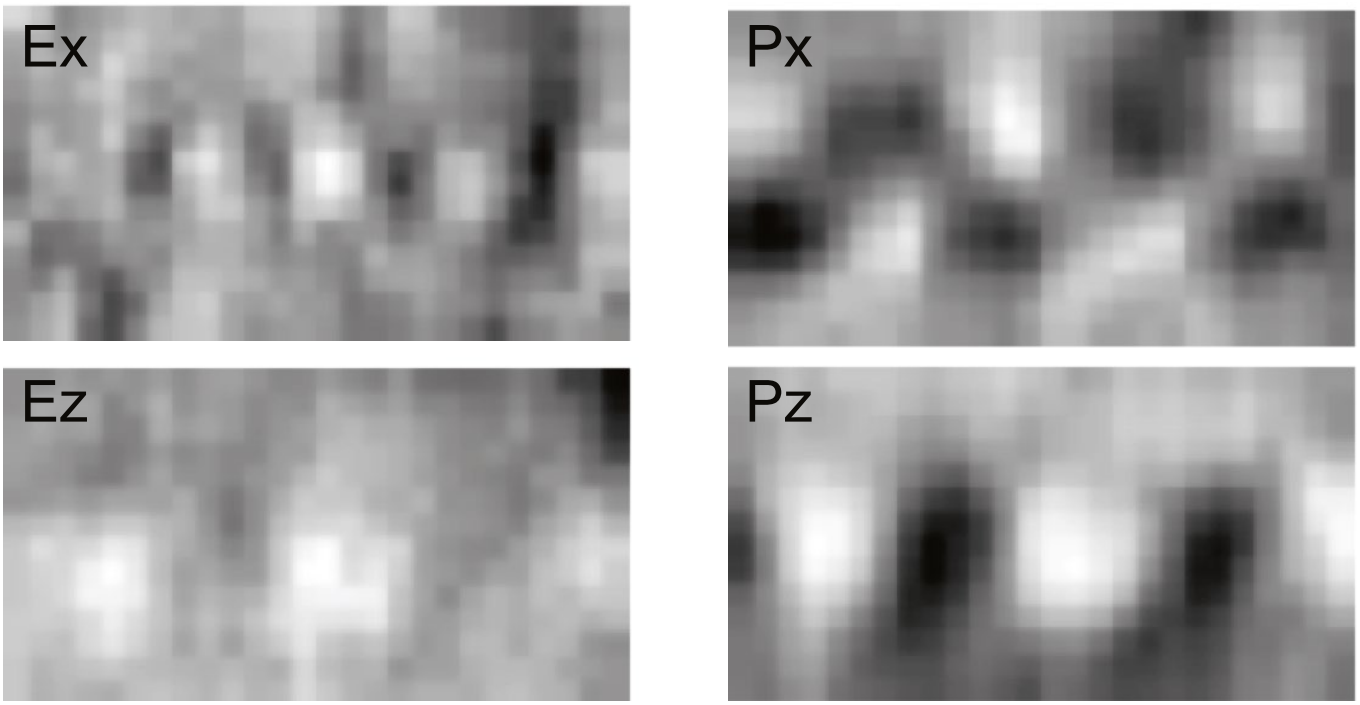

Extended Data Fig. 2 | Electric field and polarization field extracted from TEM measurements. Left column, x and z components of the electric field, E_x (top) and E_z (bottom); right column, x and z components of the polarization field, P_x (top) and P_z (bottom). $E_{x,z}$ and $P_{x,z}$ are extracted from the 4D STEM measurements of a $PbTiO_3$ multilayer in Extended Data Fig. 1, as discussed in Methods section 'EMPAD'. The electric field is determined from the center-of-mass shift of the central disk (red disk in Extended Data Fig. 1). The polarization is determined from the center of mass of the Friedel pairs (orange in Extended Data Fig. 1). Field of view, 12 nm.

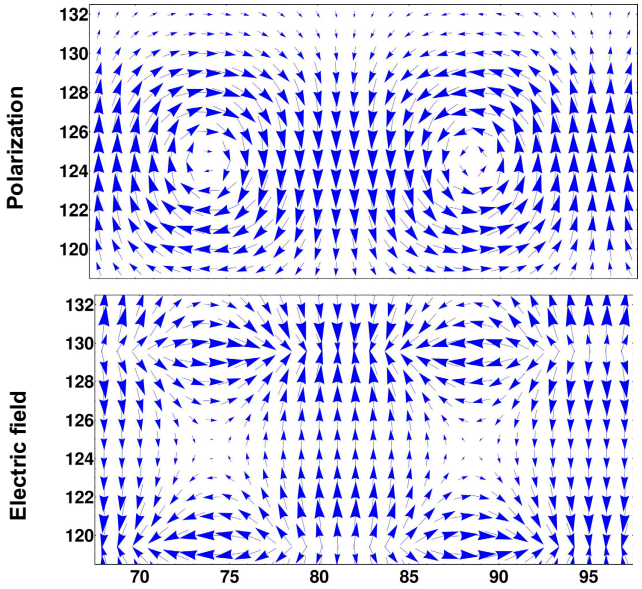

Extended Data Fig. 3 | Vector maps of the electric field and polarization field calculated from phase-field simulations. Top, polarization field; bottom, electric field.

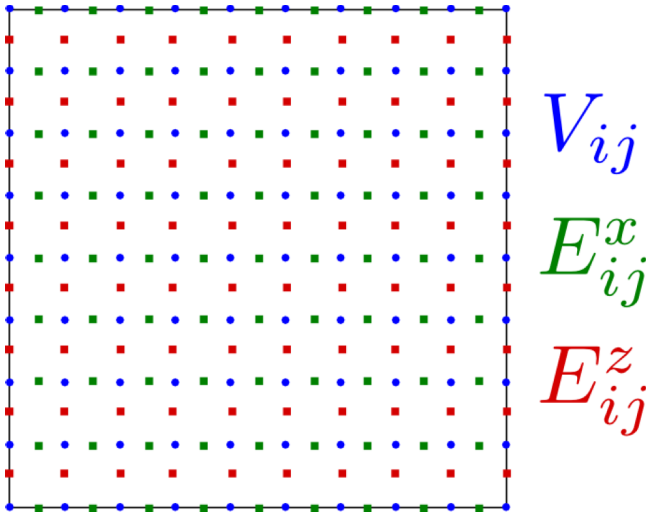

Extended Data Fig. 4 | Illustration of the grids used to obtain the local dielectric constant. The electrostatic potential is computed at the points of a regular real space grid (blue dots). Then the local electric field components along *x* and *z* are computed from finite-difference derivatives at the points of two extra staggered regular grids (green and red points).

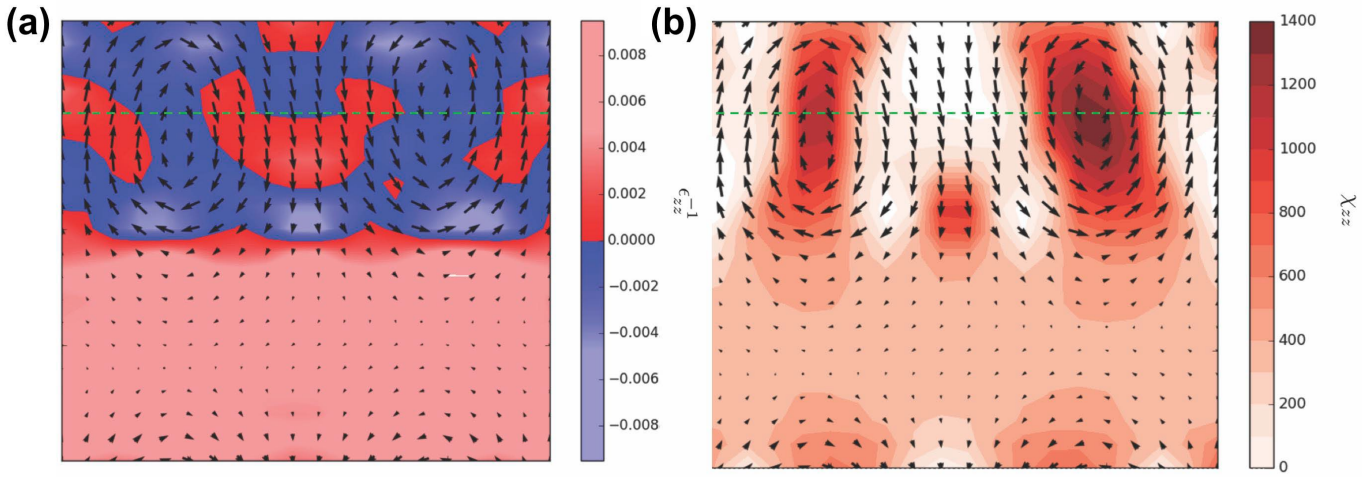

Extended Data Fig. 5 | Second-principles calculations of the 2D distribution of the inverse of the dielectric constant and the susceptibility. a, The inverse of the dielectric constant is colour-coded (key at right); **b**, the susceptibility is colour coded (key at right). Both **a** and **b** are overlaid by the polarization vectors, and the green dashed line in both panels shows the line cut used to produce Fig. 4.

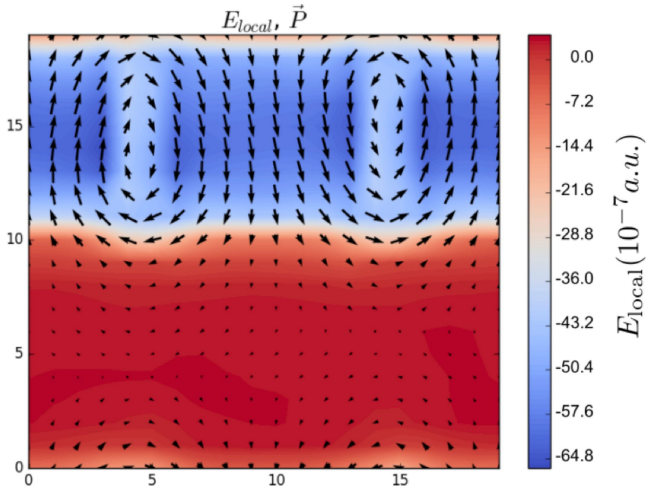

Extended Data Fig. 6 | Second-principles calculation of the local energy density map overlaid with polarization vectors. Note that within the $PbTiO_3$ layer (the top where the polarization vectors can be seen more clearly), the core region has a higher energy than the other regions (see colour key at right, in atomic units, a.u.). The core regions are also where the local permittivity is negative. The local energy in the $SrTiO_3$ layer (mostly red) is quite uniform and is equal to the reference energy. Note that the energies shown here are the differences with respect to the reference structure that corresponds to the cubic centrosymmetric phase.

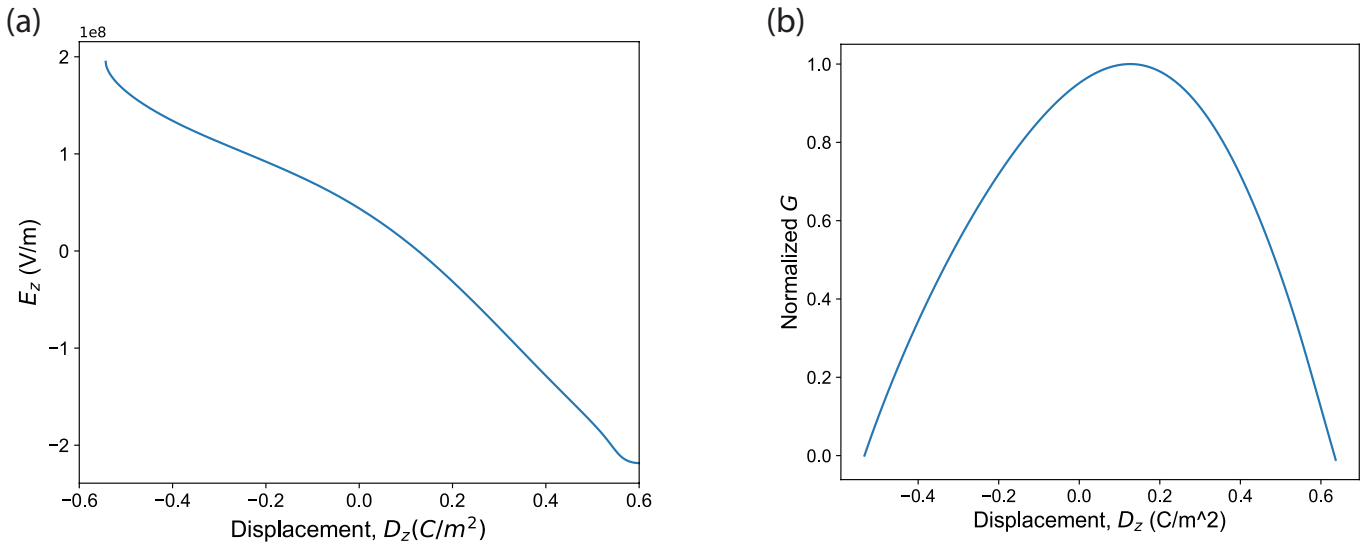

Extended Data Fig. 7 | Determination of normalized *G*. a, Plot of E_z versus D_z determined from looking at experimentally measured, varying polarization across a vortex and plotting the corresponding electric field (see Fig. 3c). **b**, Normalized G estimated from **a** using $G = \int E_z \mathrm{d}D_z$.

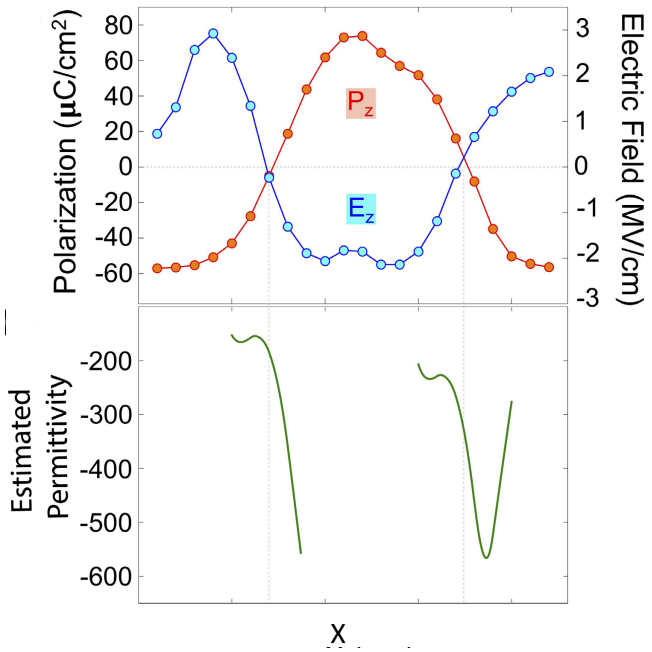

Extended Data Fig. 8 | Estimation of local permittivity. Top, z components of polarization (P_z) and of electric field (E_z), plotted against X (position along the lattice). Bottom, permittivity estimated as described in Methods. Permittivity is negative in the regions around the core.

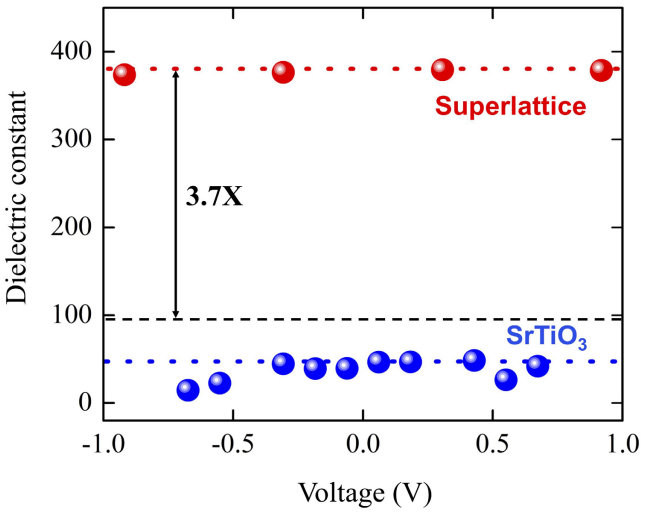

Extended Data Fig. 9 | Experimentally measured dielectric constant as a function of voltage. In red, data are shown for a 100 nm $(SrTiO_3)_{12}$/$(PbTiO_3)_{12}$ superlattice where the existence of vortex states was confirmed. In blue, for comparison, the permittivity (dielectric constant) of a 50 nm $SrTiO_3$ sample is plotted (note that the combined thickness of $SrTiO_3$ in the superlattice is also 50 nm). The black dashed line shows the threshold that needs to be surpassed for capacitance enhancement caused by a stabilized negative capacitance in the $PbTiO_3$ layer. An enhancement in permittivity of almost 3.7 times is observed compared to this threshold.